Five-Dimensional Depth-Velocity Filtering for Enhancing Moving Objects in Light Field Videos

Chamira U. S. Edussooriya, Donald G. Dansereau, *Member, IEEE,* Len T. Bruton, *Life Fellow, IEEE,* and Panajotis Agathoklis, *Senior Member, IEEE*

***Abstract*— Five-dimensional (5-D) light field video (LFV) (also known as plenoptic video) is a more powerful form of representing information of dynamic scenes compared to conventional three-dimensional (3-D) video. In this paper, the 5-D spectrum of an object in an LFV is derived for the important practical case of objects moving with constant velocity and at constant depth. In particular, it is shown that the region of support (ROS) of the 5-D spectrum is a skewed 3-D hyperfan in the 5-D frequency domain, with the degree of skew depending on the velocity and depth of the moving object. Based on this analysis, a 5-D depth-velocity digital filter to enhance moving objects in LFVs is proposed, described and implemented. Further, by means of the commercially available Lytro light-field camera, LFVs of real scenes are generated and used to test and confirm the performance of the 5-D depth-velocity filters for enhancing such objects.**

***Index Terms*— Depth-velocity filters, multidimensional filtering, light field videos, plenoptic videos, plenoptic function, spectral analysis, linear-trajectory signals.**

I. Introduction

THE seven-dimensional (7-D) plenoptic function, proposed by Adelson and Bergen [1], describes the intensity of light rays passing through the center of an ideal camera at every possible location in the three-dimensional (3-D) space (x, y, z), at every possible angle (θ, ϕ), for every wavelength λ and at every time t. The five-dimensional (5-D) light field video (LFV) (also known as plenoptic video) is a simplified form of the 7-D plenoptic function derived by assuming the intensity of a light ray does not change along its direction of propagation and the red, green and blue (RGB) colour components are used instead of the wavelength [2]. Ideally, an LFV of a dynamic scene in free space contains all information of the scene because it captures all the light rays emanating from the scene. This richness of information may be exploited to accomplish novel tasks that are not possible with conventional 3-D videos such as digital refocusing and depth-velocity filtering. In the next subsection, a brief review of previous work is presented.

This work was supported in part by the Natural Sciences and Engineering Research Council (NSERC) of Canada.

C. U. S. Edussooriya and P. Agathoklis are with the Department of Electrical and Computer Engineering, University of Victoria, Victoria, BC V8W 2Y2, Canada (e-mail: chamira@ece.uvic.ca; pan@ece.uvic.ca).

D. G. Dansereau is with the ARC Centre of Excellence for Robotic Vision, Queensland University of Technology, Brisbane QLD 4000, Australia (e-mail: donald.dansereau@qut.edu.au).

L. T. Bruton is with the Department of Electrical and Computer Engineering, University of Calgary, Calgary, AB T2N 1N4, Canada (e-mail: bruton@ucalgary.ca).

A. Related Work

3-D Linear-Trajectory Filtering: In many applications including traffic analysis, motion detection, radar tracking and computer vision, enhancement of moving objects is generally accomplished by employing 3-D velocity filters (also known as 3-D linear-trajectory filters) [3]–[7]. Such filters selectively filter moving objects based on their two-dimensional (2-D) spatial velocities. A number of design methods for 3-D velocity filters are found in the literature. In [8], a 3-D infinite-extent impulse response (IIR) filter having a planar passband has been proposed based on the concept of network resonance to enhance moving objects having linear trajectories, i.e. objects moving with constant velocities. In [9], the work presented in [8] has been extended to 3-D IIR adaptive filters for tracking and enhancing moving objects with general trajectories. Another IIR filter design technique for tracking moving objects with linear or nonlinear trajectories has been presented in [10]. In [11], an optimal 3-D finite-extent impulse response (FIR) filter for detecting moving objects with linear trajectories has been proposed. Two 3-D IIR filter banks having wedge-shaped (exterior of a wide-angle cone) passbands have been reported in [12] and [13]. An IIR velocity filter and an IIR velocity filter bank designed using multidimensional wave digital filters have been presented in [7] and [14], respectively. Recently, another low-complexity 3-D FIR filter bank has been proposed in [15].

4-D Depth Filtering: Four-dimensional (4-D) light fields (LFs) have been used for image-based rendering systems [16], [17], refocusing in digital photography [18]–[21] and exposing occluded regions in a scene [22]–[26]. Another important application is enhancing objects of a scene based on their depth. This has been first demonstrated in [27] using a 4-D depth filter having a planar passband. Similar results have been reported in [22], [28] and [29]. In particular, an efficient 4-D IIR filter was proposed in [28]. In [30], a 4-D IIR dual-fan filter is proposed to selective filtering of objects occupied in a range of depths. Two hardware implementations of first-order 4-D IIR hyper-planar filters that can be employed for depth filtering of LFs have been proposed in [31] and [32]. Furthermore, recently, differential-form and integral-form 4-D IIR depth filters and their hardware implementations have been presented in [25] and [33], respectively.

5-D Light Field Video: Most of the early work on LFVs was about capturing and rendering systems. In [34] and [35], a

system consisting of 100 conventional video cameras, arranged rectangularly on a plane, is presented. In [36], another system has been described. This system was comprised of eight conventional video cameras arranged in a line, and real-time LFV compression and decompression has also been discussed. Recently, an LFV capturing system, where conventional video cameras were arranged in a hemisphere, has been presented in [37]. This system is capable of recoding LFVs at 30 fps with a resolution of 9000×2400 pixels. A true LFV camera, especially suitable for smart phones, is reported in [38]. In the context of motion analysis in LFVs, 3-D motion estimation has been studied in [39] and [40]. In addition, recently, closed-form solutions for visual odometry for LFV cameras have been reported in [41].

Spectral Analysis of the 7-D Plenoptic Function: Some of the earliest work in spectral analysis of the plenoptic function has been presented in [42] and [43] in the context of LFs and image-based rendering. In particular, for a Lambertian scene, it is shown that the region of support (ROS) of the spectrum of an LF is bounded by the minimum and maximum depths. In [19] and [44], the ROS of the spectrum of an LF is shown to be a 3-D manifold in the 4-D frequency space, which is denoted as a 3-D hyperfan in [45]. In [46], the spectral analysis of the plenoptic function was extended to non-Lambertian and occluded scenes exploiting the concept of the so-called six-dimensional (6-D) surface plenoptic function. It is shown that non-Lambertian reflections and occlusion broaden the ROS of the spectrum of an LF. Furthermore, it was asserted that, in most cases, the spectrum is not band limited even though the surface plenoptic function may be band limited. In [47], the bandwidth of the plenoptic function has been more precisely analyzed, and show that the plenoptic function is not band limited unless the scene is a flat surface. Moreover, it is shown that the bandwidth of the plenoptic function depends on the maximum surface slope in addition to the minimum and maximum depths of the scene and the maximum frequency of the texture of the scene. In [48], the bandwidth of the plenoptic function has been examined under the finite field-of-view constraint of cameras and finite scene width. It is shown that finite constraints lead to band-unlimited plenoptic spectra even for Lambertian scenes having only a flat surface.

B. Contributions of the Paper

We analyze the spectrum of an LFV that corresponds to a Lambertian object moving with constant velocity and show that such moving objects can be enhanced based on depth and velocity by employing 5-D depth-velocity filters. To the best of our knowledge, the proposed 5-D depth-velocity filter is the first such 5-D filter applied to LFVs to enhance moving objects based on depth and velocity.

We begin the analysis by showing that a Lambertian point source moving with a constant velocity (i.e., having a linear trajectory) is represented as a 3-D hypersurface of constant value in the continuous-domain LFVs. Next, it is shown that when the motion of the Lambertian point source is parallel to the camera plane (i.e., the Lambertian point source moves at a constant depth), the 3-D hypersurface is reduced to a 3-D hyperplane. For this case, we derive the spectrum of the LFV and its ROS in closed form. The ROS of the spectrum is a plane through the origin in the 5-D frequency domain. Based on the analysis for a Lambertian point source, the ROS of the spectrum of a continuous-domain LFV, corresponding to a Lambertian object moving with a constant velocity and at a constant depth, is derived. For this case, it is shown that the ROS of the spectrum is a skewed 3-D hyperfan in the 5-D frequency domain. The degree of skew of the 3-D hyperfan depends on both velocity and depth of the moving object whereas the angle of the 3-D hyperfan depends on the depth range occupied by the moving object. Furthermore, it is shown that the essential bandwidth of the spectrum is finite along the temporal frequency dimension and, therefore, the corresponding discrete-domain LFV can be generated with negligible aliasing by employing a sufficiently high temporal sampling rate. The analysis is concluded by deriving the ROS of the spectrum for a discrete-domain LFV sampled with negligible aliasing and illustrating it through numerical simulations.

The 3-D hyperfans corresponding to the ROSs of the spectra of Lambertian objects moving with different constant velocities or at different constant depths do not overlap except at the origin in the 5-D frequency domain. This allows enhancement of such objects based on depth and velocity by employing 5-D digital filters, what we define as *depth-velocity* filters. In particular, we propose a novel 5-D depth-velocity filter having a planar passband in the 5-D frequency domain. An application of such filters is presented, where a moving object of interest in an LFV (generated by employing a commercially available Lytro LF camera) is enhanced while attenuating other interfering moving objects. Experimental results indicate that the proposed 5-D depth-velocity filters are capable of enhancing moving objects and exposing occluded regions of a scene. Consequently, they are of significant interest for many applications such as digital video photography, surveillance and security systems, and various applications in computer vision.

C. Outline of the Paper

The rest of the paper is organized as follows. In Section II, LF representation of a Lambertian scene and its spectrum are briefly reviewed. In Section III, the spectrum of an LFV containing Lambertian objects moving with constant velocity and at constant depth is analyzed. The design and implementation of an appropriate 5-D depth-velocity filter that can be employed to enhance moving objects in an LFV are presented in Section IV. Furthermore, we present experimental results obtained for an LFV of a real scene in Section IV. In Section V, we briefly discuss effects of non-Lambertian reflections and occlusion on the enhancement of moving objects in an LFV by employing 5-D depth-velocity filters and a strategy to enhance Lambertian objects moving at non-constant depth. Finally, conclusions and future work are presented in Section VI.

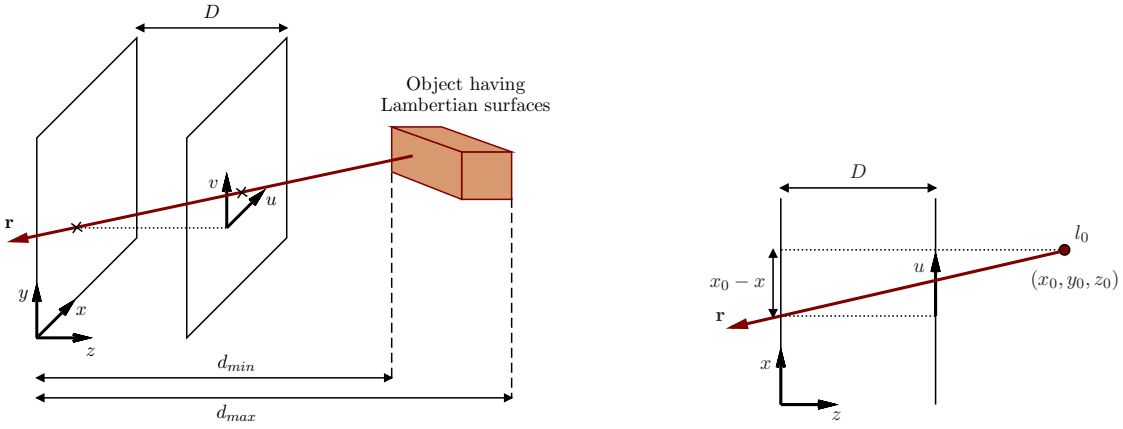

Fig. 1. (a) The two-plane parameterization of a Lambertian scene comprised of an object having Lambertian surfaces; (b) the parameterization of a Lambertian point source of intensity l_0 in the xu subspace.

II. Review of LF Representation of a Lambertian Scene and Its Spectrum

We briefly review the LF representation of a Lambertian scene and its spectrum, i.e. the Fourier transform, in this section. To this end, we consider the standard two-plane parameterization [16] of a simple Lambertian scene as shown in Fig. 1. Note that, in the case of a camera array, the camera plane xy corresponds to the plane containing the principal planes of the camera lenses, and the image plane uv corresponds to the coplanar focal planes of the cameras. For simplicity, the scene is assumed to have no occlusion. Furthermore, windowing effects due to the finite number of cameras and due to the limited field-of-view of each camera are ignored, i.e. both the camera plane xy and the image plane uv are of infinite extent. Also note that the image coordinate (u, v) is defined locally with respect to the camera position (x, y). In the two-plane parameterization, the pinhole camera model is assumed, and each ray $\mathbf{r}$ is parameterized by its intersections with the xy and uv planes. In other words, each ray $\mathbf{r}$ is represented by the 4-tuple $(x, y, u, v) \in \mathbb{R}^4$, where the coordinates (x, y) and (u, v) represent the position and direction of the ray, respectively.

The simple scene illustrated in Fig. 1 is comprised of an object having Lambertian surfaces [49](ch. 2.2). A Lambertian surface may be considered as a collection of Lambertian point sources and, therefore, the LF of a Lambertian object is given by the superposition of the LFs of corresponding Lambertian point sources. Consequently, in the following review and in the analysis presented in Section III, we mainly pay our attention to the LF and LFV representation of *Lambertian point sources*.

The 4-D continuous-domain LF $l_{4\mathrm{C}}(x, y, u, v)$ corresponding to a Lambertian point source is a plane of constant value l_0, where l_0 is the intensity (or radiance) of the Lambertian point source. The plane is given by the intersection of the two 3-D hyperplanes

$$mx + u + c_x = 0 \tag{1a}$$
$$my + v + c_y = 0, \tag{1b}$$

having normal vectors $[m, 0, 1, 0]^{\mathrm{T}}$ and $[0, m, 0, 1]^{\mathrm{T}}$, respectively, where

$$m = \frac{D}{z_0} \tag{2a}$$
$$c_x = \frac{-Dx_0}{z_0} \tag{2b}$$
$$c_y = \frac{-Dy_0}{z_0}, \tag{2c}$$

where $(x_0, y_0, z_0) \in \mathbb{R}^2 \times \mathbb{R}^+$ is the position of the Lambertian point source and D is the distance between the camera plane xy and the image plane uv [28]. Here and in the rest of the paper, an n-D hyperplane, where $n = 3, 4$, means an n-D manifold in the $(n+1)$-D space that is uniquely determined by the $(n+1)$-D normal vector and an $(n+1)$-D point on the n-D hyperplane. The LF $l_{4\mathrm{C}}(x, y, u, v)$ may be expressed as

$$l_{4\mathrm{C}}(x, y, u, v) = l_0\, \delta(mx + u + c_x)\, \delta(my + v + c_y), \tag{3}$$

where $\delta(\cdot)$ is the one-dimensional (1-D) continuous-domain impulse function.

The spectrum of $l_{4\mathrm{C}}(x, y, u, v)$, $L_{4\mathrm{C}}(\Omega_x, \Omega_y, \Omega_u, \Omega_v)$, and its ROS $\mathcal{P}_{4\mathrm{C}}$ are obtained as [28], [43]

$$L_{4\mathrm{C}}(\Omega_x, \Omega_y, \Omega_u, \Omega_v) = 4\pi^2 l_0\, \delta(\Omega_x - m\Omega_u)\, \delta(\Omega_y - m\Omega_v) \times \mathrm{e}^{j(\Omega_u c_x + \Omega_v c_y)} \tag{4}$$

and

$$\mathcal{P}_{4\mathrm{C}} = \mathcal{H}_{4\mathrm{C},xu} \cap \mathcal{H}_{4\mathrm{C},yv}, \tag{5}$$

respectively, where $(\Omega_x, \Omega_y, \Omega_u, \Omega_v) \in \mathbb{R}^4$ and

$$\mathcal{H}_{4\mathrm{C},xu} = \{(\Omega_x, \Omega_y, \Omega_u, \Omega_v) \in \mathbb{R}^4 \mid \Omega_x - m\Omega_u = 0\} \tag{6a}$$
$$\mathcal{H}_{4\mathrm{C},yv} = \{(\Omega_x, \Omega_y, \Omega_u, \Omega_v) \in \mathbb{R}^4 \mid \Omega_y - m\Omega_v = 0\}. \tag{6b}$$

The ROS $\mathcal{P}_{4\mathrm{C}}$ is a plane through the origin in the 4-D continuous frequency domain, which is given by the intersection of the two 3-D hyperplanes

$$\Omega_x - m\Omega_u = 0 \tag{7a}$$
$$\Omega_y - m\Omega_v = 0 \tag{7b}$$

having normal vectors $[1, 0, -m, 0]^{\mathrm{T}}$ and $[0, 1, 0, -m]^{\mathrm{T}}$, respectively. The ROS $\mathcal{P}_{4\mathrm{C}}$ depends only on the depth z_0 of

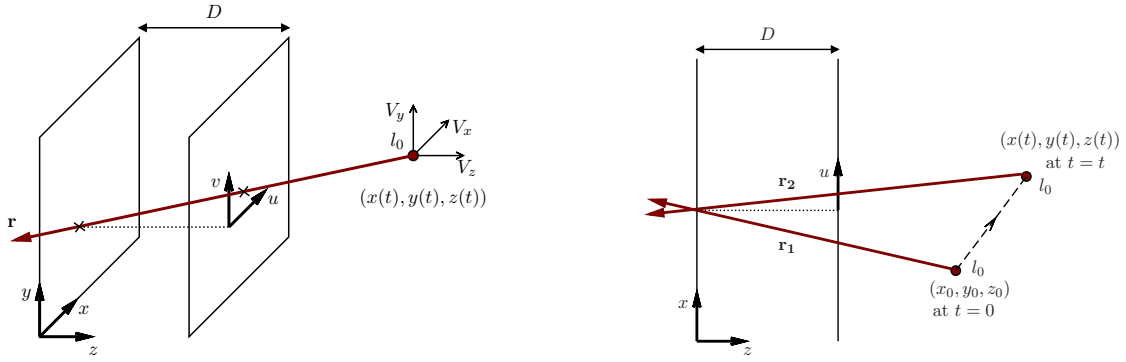

(a) (b)

Fig. 2. (a) A Lambertian point source of intensity l_0 moves with the constant velocity $\mathbf{V} = [V_x, V_y, V_z]^{\mathrm{T}}$; (b) the representation of the Lambertian point source in the xu subspace.

the Lambertian point source [28], [43]. In the case of a Lambertian object, where the depth varies in a range, i.e. $z_0 \in [d_{min}, d_{max}]$ (see Fig. 1), the ROS of the spectrum, $\mathcal{O}_{4\mathrm{C}}$, is obtained as

$$\begin{aligned}\mathcal{O}_{4\mathrm{C}} &= \bigcup_{z_0} \mathcal{P}_{4\mathrm{C}} \\ &= \bigcup_{z_0} \left(\mathcal{H}_{4\mathrm{C},xu} \cap \mathcal{H}_{4\mathrm{C},yv}\right), \end{aligned} \tag{8}$$

which is a 3-D hyperfan in the 4-D continuous frequency domain [45].

III. Analysis of the Spectrum of a Lambertian Object Moving with Constant Velocity

A. LFV Representation of a Lambertian Point Source

Consider the case shown in Fig. 2, where a Lambertian point source of intensity l_0 moves with the *constant* velocity $\mathbf{V} = [V_x, V_y, V_z]^{\mathrm{T}}$. Similar to the 4-D continuous-domain LF representation of a Lambertian point source, as discussed in the previous section, the 5-D continuous-domain LFV $l_{5\mathrm{C}}(\mathbf{x})$, $\mathbf{x} = [x, y, u, v, t]^{\mathrm{T}} \in \mathbb{R}^5$, may be expressed as

$$l_{5\mathrm{C}}(\mathbf{x}) = l_0\, \delta(m(t)x + u + c_x(t))\, \delta(m(t)y + v + c_y(t)), \tag{9}$$

where

$$m(t) = \frac{D}{z(t)} \tag{10a}$$

$$c_x(t) = \frac{-Dx(t)}{z(t)} \tag{10b}$$

$$c_y(t) = \frac{-Dy(t)}{z(t)}. \tag{10c}$$

In this case, similar to the *constant intensity assumption* [50](ch. 2.3) employed in analysis of moving objects in conventional 3-D videos, we assume that the intensity l_0 of the Lambertian point source does not change with time, i.e. the scene is under *homogeneous ambient illumination*. Because

$$x(t) = V_x t + x_0 \tag{11a}$$

$$y(t) = V_y t + y_0 \tag{11b}$$

$$z(t) = V_z t + z_0, \tag{11c}$$

where $(x_0, y_0, z_0) \in \mathbb{R}^2 \times \mathbb{R}^+$ is the position of the Lambertian point source at $t = 0$, after some manipulation, (9) can be rewritten as

$$\begin{aligned} l_{5\mathrm{C}}(\mathbf{x}) = l_0\, &\delta(mx + u + k_x t - k_z ut + c_x) \\ &\times \delta(my + v + k_y t - k_z vt + c_y), \end{aligned} \tag{12}$$

where m, c_x and c_y are given by (2a), (2b) and (2c), respectively, and

$$k_x = \frac{-DV_x}{z_0} \tag{13a}$$

$$k_y = \frac{-DV_y}{z_0} \tag{13b}$$

$$k_z = \frac{-V_z}{z_0}. \tag{13c}$$

According to (12), the Lambertian point source is represented in the LFV $l_{5\mathrm{C}}(\mathbf{x})$ as a *3-D hypersurface of constant value* l_0, which is given by the intersection of the two 4-D hypersurfaces

$$mx + u + k_x t - k_z ut + c_x = 0 \tag{14a}$$

$$my + v + k_y t - k_z vt + c_y = 0. \tag{14b}$$

In the case, where the Lambertian point source moves at a *constant depth* z_0, i.e. $V_z = 0$, (12) reduces to

$$\begin{aligned} l_{5\mathrm{C}}(\mathbf{x}) = l_0\, &\delta(mx + u + k_x t + c_x) \\ &\times \delta(my + v + k_y t + c_y). \end{aligned} \tag{15}$$

In this case, the Lambertian point source is represented in the LFV $l_{5\mathrm{C}}(\mathbf{x})$ as a *3-D hyperplane of constant value* l_0, which is given by the intersection of the two 4-D hyperplanes

$$mx + u + k_x t + c_x = 0 \tag{16a}$$

$$my + v + k_y t + c_y = 0 \tag{16b}$$

having normal vectors $[m, 0, 1, 0, k_x]^{\mathrm{T}}$ and $[0, m, 0, 1, k_y]^{\mathrm{T}}$, respectively.

B. Spectrum of a Lambertian Point Source Moving at a Constant Depth

In this subsection, the spectrum of $l_{5\mathrm{C}}(\mathbf{x})$ is derived in closed form for the case $V_z = 0$. The spectrum $L_{5\mathrm{C}}(\mathbf{\Omega})$,

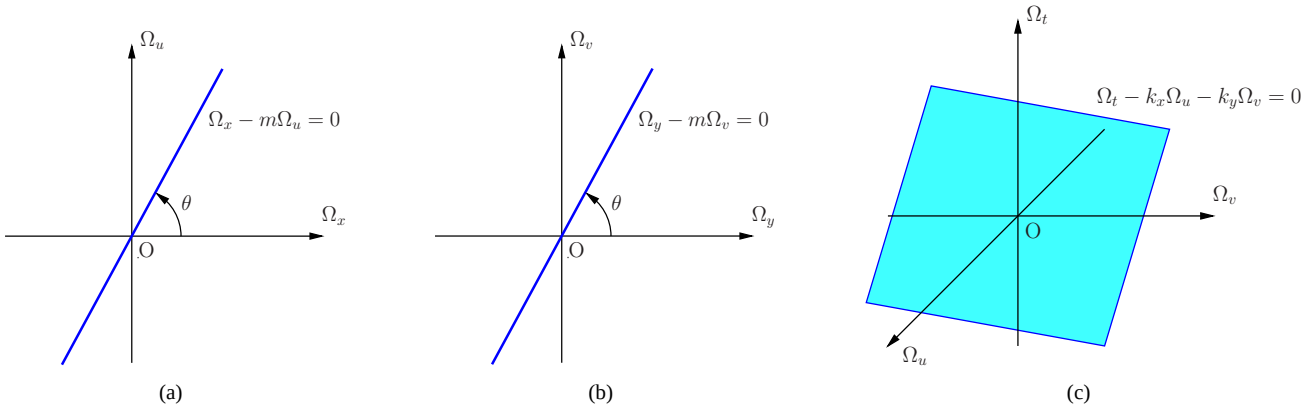

Fig. 3. The ROS of the spectrum, $\mathcal{P}_{5\mathrm{C}}$, (a) $\mathcal{H}_{5\mathrm{C},xu}$ in the $\Omega_x\Omega_u$ subspace; (b) $\mathcal{H}_{5\mathrm{C},yv}$ in the $\Omega_y\Omega_v$ subspace; as z_0 varies in the range $(0,\infty)$, θ varies in the range $(0°, 90°)$. (c) $\mathcal{H}_{5\mathrm{C},uvt}$ in the $\Omega_u\Omega_v\Omega_t$ subspace.

$\mathbf{\Omega} = [\Omega_x, \Omega_y, \Omega_u, \Omega_v, \Omega_t]^{\mathrm{T}} \in \mathbb{R}^5$, can be obtained as

$$L_{5\mathrm{C}}(\mathbf{\Omega}) = 8\pi^3 l_0\, \delta(\Omega_x - m\Omega_u)\, \delta(\Omega_y - m\Omega_v) \times \delta(\Omega_t - k_x\Omega_u - k_y\Omega_v)\, \mathrm{e}^{j(\Omega_u c_x + \Omega_v c_y)} \quad (17)$$

as derived in Appendix I. Note that, similar to the spectrum of an object moving with constant 2-D spatial velocity in a conventional 3-D video [50](ch. 2.3), (17) can be expressed as

$$L_{5\mathrm{C}}(\mathbf{\Omega}) = 2\pi\, L_{4\mathrm{C}}(\Omega_x, \Omega_y, \Omega_u, \Omega_v) \times \delta(\Omega_t - k_x\Omega_u - k_y\Omega_v), \quad (18)$$

where $L_{4\mathrm{C}}(\Omega_x, \Omega_y, \Omega_u, \Omega_v)$ is the spectrum of the *time-invariant* LF of the Lambertian point source as given in (4).

From (17), the ROS of the spectrum, $\mathcal{P}_{5\mathrm{C}}$, can be obtained as

$$\mathcal{P}_{5\mathrm{C}} = \mathcal{H}_{5\mathrm{C},xu} \cap \mathcal{H}_{5\mathrm{C},yv} \cap \mathcal{H}_{5\mathrm{C},uvt}, \quad (19)$$

where

$$\mathcal{H}_{5\mathrm{C},xu} = \{\mathbf{\Omega} \in \mathbb{R}^5 \mid \Omega_x - m\Omega_u = 0\} \quad (20a)$$
$$\mathcal{H}_{5\mathrm{C},yv} = \{\mathbf{\Omega} \in \mathbb{R}^5 \mid \Omega_y - m\Omega_v = 0\} \quad (20b)$$
$$\mathcal{H}_{5\mathrm{C},uvt} = \{\mathbf{\Omega} \in \mathbb{R}^5 \mid \Omega_t - k_x\Omega_u - k_y\Omega_v = 0\}, \quad (20c)$$

which are illustrated in Figs. 3(a)–3(c), respectively. The ROS $\mathcal{P}_{5\mathrm{C}}$ is a *plane through the origin* in the 5-D continuous frequency domain, which is given by the intersection of the three 4-D hyperplanes

$$\Omega_x - m\Omega_u = 0 \quad (21a)$$
$$\Omega_y - m\Omega_v = 0 \quad (21b)$$
$$\Omega_t - k_x\Omega_u - k_y\Omega_v = 0 \quad (21c)$$

having normal vectors $[1, 0, -m, 0, 0]^{\mathrm{T}}$, $[0, 1, 0, -m, 0]^{\mathrm{T}}$ and $[0, 0, -k_x, -k_y, 1]^{\mathrm{T}}$, respectively. Note that the ROS $\mathcal{P}_{5\mathrm{C}}$ depends on both the constant velocity vector $\mathbf{V} = [V_x, V_y, 0]^{\mathrm{T}}$ and the depth z_0 of the Lambertian point source, implying that Lambertian point sources moving with different constant velocities or at different depths ideally have *non-overlapping* ROSs except at the origin. This fact is the basis for enhancing moving objects in LFVs by employing 5-D depth-velocity filters described in Section IV.

C. ROS of the Spectrum of a Lambertian Object Moving at a Constant Depth

In the context of filter design, the ROS of the spectrum is more important than the spectrum itself since the most of the design specifications, such as cutoff frequencies, of a filter are determined based on the ROS of the spectra of signals to be filtered. In this subsection, we derive the ROS of the spectrum of a Lambertian object moving with $\mathbf{V} = [V_x, V_y, 0]^{\mathrm{T}}$.

The Lambertian object may be considered as a collection of Lambertian point sources having depth $z_0 \in [d_{min}, d_{max}]$ (see Fig. 1). Therefore, the ROS of the spectrum, $\mathcal{O}_{5\mathrm{C}}$, can be obtained as the *union* of the ROSs of the spectra of the corresponding Lambertian point sources because of the linearity of the Fourier transform [51](ch. 1.3), i.e.

$$\mathcal{O}_{5\mathrm{C}} = \bigcup_{z_0} \mathcal{P}_{5\mathrm{C}} = \bigcup_{z_0} (\mathcal{H}_{5\mathrm{C},xu} \cap \mathcal{H}_{5\mathrm{C},yv} \cap \mathcal{H}_{5\mathrm{C},uvt})\,. \quad (22)$$

The ROS $\mathcal{O}_{5\mathrm{C}}$ is a *skewed 3-D hyperfan* in the 5-D continuous frequency domain. Here, 3-D hyperfan means a 3-D manifold that can be formed by sweeping a plane through the 4-D or 5-D space. The degree of skew of the 3-D hyperfan depends on both velocity and depth of the moving object whereas the angle of the 3-D hyperfan depends on the depth range occupied by the moving object. Note that, similar to 4D LFs, we observe a *dimensionality gap* in the ROS of the spectrum; that is the 5-D LFV is reduced to a 3-D manifold in the 5-D continuous frequency domain. In this case, one dimension is reduced due to the fact that the Lambertian scene is in fact in the 3-D space though represented as 4-D in the corresponding LF [44]. In other words, the parameter m in (16a) and (16b) is the same for both 4-D hyperplanes for a point in the 3-D space. The other dimension is reduced as a consequence of the constant intensity assumption.

D. ROS of the Spectrum Corresponding to a Discrete-Domain LFV

An LFV obtained from an LFV camera is in fact a discrete-domain (sampled) signal. Consequently, processing of LFVs

is carried out in the discrete-domain. In this subsection, we derive the ROS of the spectrum corresponding to a *discrete-domain* LFV. To this end, we assume that the discrete-domain LFV $l_{5\mathrm{D}}(\mathbf{n})$, $\mathbf{n} = [n_x, n_y, n_u, n_v, n_t]^{\mathrm{T}} \in \mathbb{Z}^5$, is generated by rectangularly sampling the corresponding continuous-domain LFV $l_{5\mathrm{C}}(\mathbf{x})$, with the sampling matrix

$$\boldsymbol{\Delta} = \mathrm{diag}[\Delta x, \Delta y, \Delta u, \Delta v, \Delta t], \tag{23}$$

where the term "diag" denotes a diagonal matrix and Δi, $i = x, y, u, v, t$, is the sampling interval along the corresponding dimension. Furthermore, the *5-D principal Nyquist hypercube* in the 5-D discrete frequency domain $\boldsymbol{\omega}$ $(= [\omega_x, \omega_y, \omega_u, \omega_v, \omega_t]^{\mathrm{T}} \in \mathbb{R}^5$, where $\omega_i = \Omega_i \Delta i$, $i = x, y, u, v, t)$ is defined as

$$\mathcal{N} \triangleq \left\{ \boldsymbol{\omega} \in \mathbb{R}^5 \mid -\pi \leq \omega_i \leq \pi,\ i = x, y, u, v, t \right\}. \tag{24}$$

The discrete-domain spectrum $L_{5\mathrm{D}}(\boldsymbol{\omega})$ is a periodic extension of the corresponding continuous-domain spectrum $L_{5\mathrm{D}}(\boldsymbol{\Omega})$ and is given by [51](ch. 1.4)

$$L_{5\mathrm{D}}(\boldsymbol{\omega}) = \frac{1}{|\mathrm{det}\boldsymbol{\Delta}|} \sum_{\mathbf{k}} L_{5\mathrm{C}} \left(\boldsymbol{\Omega} - 2\pi \boldsymbol{\Delta}^{-1} \mathbf{k} \right), \tag{25}$$

where $\mathbf{k} \in \mathbb{Z}^5$ and the term "det" denotes the determinant of a matrix. Even though the spectrum of an LF is, in general, band unlimited, most of the energy of the spectrum resides within a finite 4-D hypervolume denoted as the *essential bandwidth* [47], [48]. Therefore, most LFs can be sampled with negligible aliasing. It is clear from (17) and especially from (18) that the maximum temporal frequency of $L_{5\mathrm{C}}(\boldsymbol{\Omega})$ depends only on the maximum values of k_x and k_y, and the essential bandwidth of $L_{4\mathrm{C}}(\Omega_x, \Omega_y, \Omega_u, \Omega_v)$ on the Ω_u and Ω_v dimensions. Consequently, with finite k_x and k_y, we can conclude that the essential bandwidth of $L_{5\mathrm{C}}(\boldsymbol{\Omega})$ on the Ω_t dimension is *finite*. Therefore, the continuous-domain LFV $l_{5\mathrm{C}}(\mathbf{x})$ can be sampled with negligible aliasing by employing a sufficiently high temporal sampling rate and, for this case, the ROS of the spectrum, $\mathcal{O}_{5\mathrm{D}}$, inside $\mathcal{N}$ is obtained as

$$\mathcal{O}_{5\mathrm{D}} = \bigcup_{z_0} \left(\mathcal{H}_{5\mathrm{D},xu} \cap \mathcal{H}_{5\mathrm{D},yv} \cap \mathcal{H}_{5\mathrm{D},uvt} \right), \tag{26}$$

where

$$\mathcal{H}_{5\mathrm{D},xu} = \left\{ \boldsymbol{\omega} \in \mathcal{N} \,\middle|\, \omega_x - \left(\frac{m\Delta x}{\Delta u} \right) \omega_u = 0 \right\} \tag{27a}$$

$$\mathcal{H}_{5\mathrm{D},yv} = \left\{ \boldsymbol{\omega} \in \mathcal{N} \,\middle|\, \omega_y - \left(\frac{m\Delta y}{\Delta v} \right) \omega_v = 0 \right\} \tag{27b}$$

$$\mathcal{H}_{5\mathrm{D},uvt} = \left\{ \boldsymbol{\omega} \in \mathcal{N} \,\middle|\, \omega_t - \left(\frac{k_x \Delta t}{\Delta u} \right) \omega_u - \left(\frac{k_y \Delta t}{\Delta v} \right) \omega_v = 0 \right\}. \tag{27c}$$

E. Numerical Simulation of the ROS of the Spectrum

In this subsection, we present the numerically simulated ROS of the spectrum of a discrete-domain LFV that corresponds to a Lambertian object moving with a constant velocity and at a constant depth. Note that, for illustration purposes, the LFV is restricted to the x, u and t dimensions. The time-invariant intensity pattern of the Lambertian object is selected as sinusoidal and the velocity V_x is selected as 3 pixels/frame. Furthermore, the distance D between the camera plane xy and the image plane uv is selected as 50 cm, and the Lambertian object occupies the depth range $[30, 70]$ cm. The LFV of size $256 \times 128 \times 64$ is numerically generated. The epipolar-plane images [52] corresponding to 10th and 40th frames of the LFV are shown in Figs. 4 (a) and 4 (b), respectively.

In the present case, where only the x, u and t dimensions are incorporated, the ROS of the spectrum, $\mathcal{O}_{3\mathrm{D}}$, inside $\mathcal{N}$ can be obtained, by following a procedure similar to that employed in the previous subsection, as

$$\mathcal{O}_{3\mathrm{D}} = \bigcup_{z_0} \left(\mathcal{H}_{3\mathrm{D},xu} \cap \mathcal{H}_{3\mathrm{D},ut} \right), \tag{28}$$

where

$$\mathcal{H}_{3\mathrm{D},xu} = \left\{ \boldsymbol{\omega} \in \mathcal{N} \,\middle|\, \omega_x - \left(\frac{m\Delta x}{\Delta u} \right) \omega_u = 0 \right\} \tag{29a}$$

$$\mathcal{H}_{3\mathrm{D},ut} = \left\{ \boldsymbol{\omega} \in \mathcal{N} \,\middle|\, \omega_t - \left(\frac{k_x \Delta t}{\Delta u} \right) \omega_u = 0 \right\}. \tag{29b}$$

Note that, in this case, $\boldsymbol{\omega} = [\omega_x, \omega_u, \omega_t]^{\mathrm{T}} \in \mathbb{R}^3$ and $\mathcal{N}$ is the principal Nyquist cube in the 3-D discrete frequency domain. The ROS of the spectrum corresponding to a single depth z_0 is a straight line through the origin of which the orientation is determined by the depth z_0 and the velocity V_x. For a Lambertian object where depth $z_0 \in [d_{min}, d_{max}]$, the ROS is a collection of straight lines that resembles a skewed fan-shaped surface inside $\mathcal{N}$, with the degree of skew depending on the velocity and depth. For example, for $V_x = 0$, the fan lies on the $\omega_x \omega_u$ plane, and when V_x increases, the angle between the fan and the $\omega_x \omega_u$ plane increases.

The ROS of the spectrum of the numerically generated LFV is shown in Fig. 5. It is observed that the ROS of the spectrum is approximately a fan-shaped surface inside $\mathcal{N}$. Consequently, the numerically obtained ROS of the spectrum is consistent with the theoretically predicted ROS of the spectrum. The slight deviations of the numerically obtained ROS of the spectrum from an ideal fan-shaped surface are mainly due to windowing effects caused by the finite number of samples available for x and u dimensions.

IV. Enhancing Moving Objects Using 5-D Depth-Velocity Filters: Experimental Results

It is clear from the spectral analysis presented in Section III that the ROSs of the spectra of objects moving with different constant velocities or at different depths are distinct and do not overlap except at the origin. Consequently, by employing a 5-D depth-velocity filter of which the passband encompasses the ROS of the spectrum of the object of interest and the stopband encompasses the ROSs of the spectra of interfering objects, the object of interest can be enhanced while attenuating the interfering objects. In this section, we present experimental results obtained for an LFV of a real scene, where 5-D depth-velocity filters are employed to enhance moving objects of interest while attenuating other interfering moving objects that move with different velocities or at different depths.

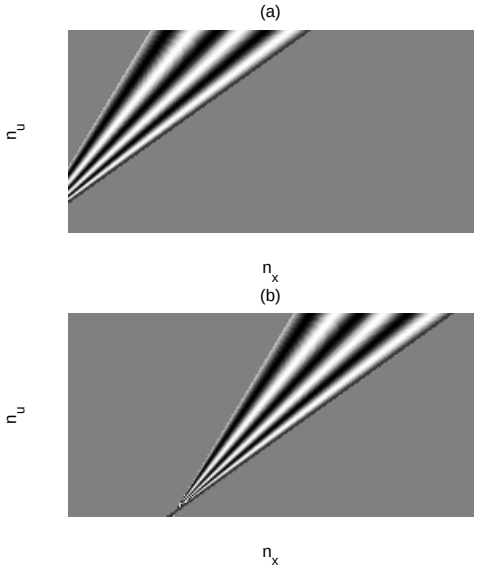

Fig. 4. The epipolar-plane images of the generated LFV (a) 10th frame; (b) 40th frame.

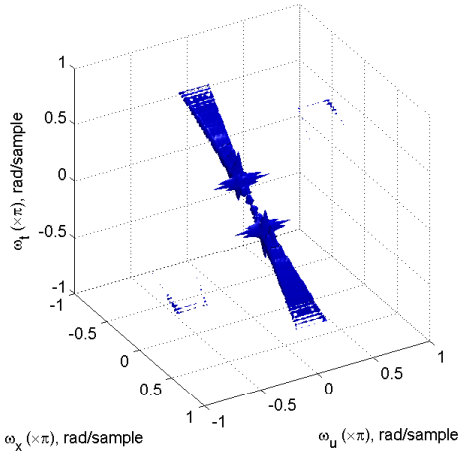

Fig. 5. The ROS of the spectrum of the numerically generated LFV. The magnitude of the spectrum is normalized, and the iso-surface is drawn at 0.05.

A. Experimental Setup and Generation of the LFV

The experimental setup, shown in Fig. 6, is comprised of a blue car (object of interest), and a red and an orange trucks (interfering objects). All three vehicles were manually moved in planes approximately parallel to the camera plane and a commercially available Lytro LF camera [53] was employed to capture static LFs of the scene. The scene is under homogeneous ambient illumination so that specular reflections are minimum. The depth ranges occupied by the blue car, red truck and the orange truck are $[160, 163]$ cm, $[157, 160]$ cm and $[108.5, 111.5]$ cm, respectively. The blue car and orange truck were manually moved from left to right with the speed of 1 cm per frame whereas the red truck was manually moved from right to left with the speed of 1 cm per frame. Note that the red truck moves at approximately the same depth of the blue car so that the red truck is very difficult to be attenuated by using 4-D depth filters. On the other hand, the orange truck

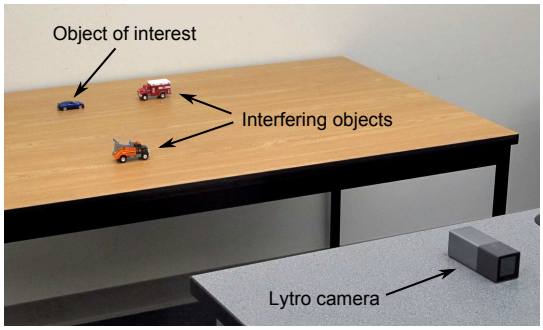

Fig. 6. The experimental setup employed to generate the LFV. A Lytro LF camera was employed to capture individual frames of the scene.The blue car (object of interest) and the red truck (interfering object) move at approximately the same depth whereas the blue car and the orange truck (interfering object) move with approximately the same velocity.

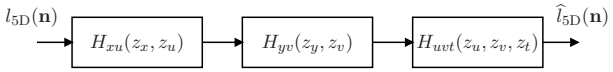

Fig. 7. Structure of the 5-D depth-velocity filter.

moves with approximately the same velocity of the blue car so that the orange truck is very difficult to be attenuated by using 3-D velocity filters. Sixty four LFs were captured, and each LF was decoded by using the LFP File Reader (Version 2.0) [54] and the MATLAB LFToolbox (Version 0.2) [55]. The generated LFV is of the size $9 \times 9 \times 370 \times 256 \times 64$.

B. Design of the 5-D Depth-Velocity Filter

The 5-D depth-velocity filter $H(\mathbf{z})$, $[z_x, z_y, z_u, z_v, z_t]^{\mathrm{T}} \in \mathbb{C}^5$ is designed as a cascade of two 2-D filters, $H_{xu}(z_x, z_u)$ and $H_{yv}(z_y, z_v)$, and a one 3-D filter, $H_{uvt}(z_u, z_v, z_t)$ as shown in Fig. 7. The passband of each of the three filters is selected as 4-D hyperplanes inside the 5-D principal Nyquist hypercube $\mathcal{N}$. In particular, the passbands of $H_{xu}(z_x, z_u)$, $H_{yv}(z_y, z_v)$ and $H_{uvt}(z_u, z_v, z_t)$ encompass the 5-D hypervolumes given by

$$\mathcal{B}_{xu} = \bigcup_{z_0} \mathcal{H}_{5\mathrm{D},xu} \tag{30a}$$

$$\mathcal{B}_{yv} = \bigcup_{z_0} \mathcal{H}_{5\mathrm{D},yv} \tag{30b}$$

$$\mathcal{B}_{uvt} = \bigcup_{z_0} \mathcal{H}_{5\mathrm{D},uvt} \tag{30c}$$

respectively, as illustrated in Fig. 8. Here, $\mathcal{H}_{5\mathrm{D},xu}$, $\mathcal{H}_{5\mathrm{D},yv}$ and $\mathcal{H}_{5\mathrm{D},uvt}$, given by (27a), (27b) and (27c), respectively, are the 4-D hyperplanes corresponding to the ROS of the spectrum of the object of interest. The overall passband $\mathcal{B}$ of $H(\mathbf{z})$, which is a plane inside the 5-D principal Nyquist hypercube $\mathcal{N}$, is given by the intersection of $\mathcal{B}_{xu}$, $\mathcal{B}_{yv}$ and $\mathcal{B}_{uvt}$, i.e.

$$\mathcal{B} = \left(\bigcup_{z_0} \mathcal{H}_{5\mathrm{D},xu}\right) \bigcap \left(\bigcup_{z_0} \mathcal{H}_{5\mathrm{D},yv}\right) \bigcap \left(\bigcup_{z_0} \mathcal{H}_{5\mathrm{D},uvt}\right). \tag{31}$$

Note that, the 3-D hyperfan corresponding to the ROS of the spectrum of the object of interest, given by (26), is a *proper*

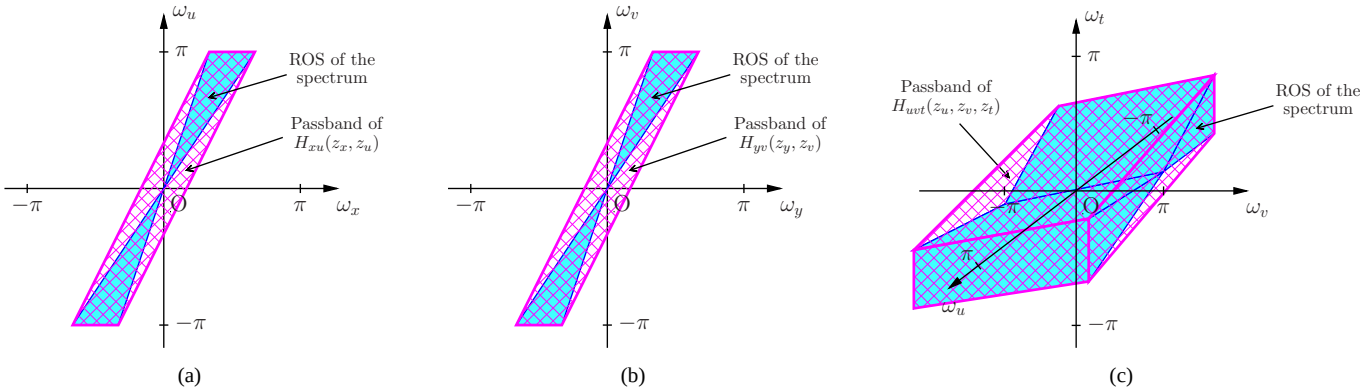

Fig. 8. The ROS of the spectrum of the object of interest (solid) and the passband (cross-hatched) of (a) $H_{xu}(z_x, z_u)$ on the $\omega_x\omega_u$ plane; (b) $H_{yv}(z_y, z_v)$ on the $\omega_y\omega_v$ plane; (c) $H_{uvt}(z_u, z_v, z_t)$ in the $\omega_u\omega_v\omega_t$ space.

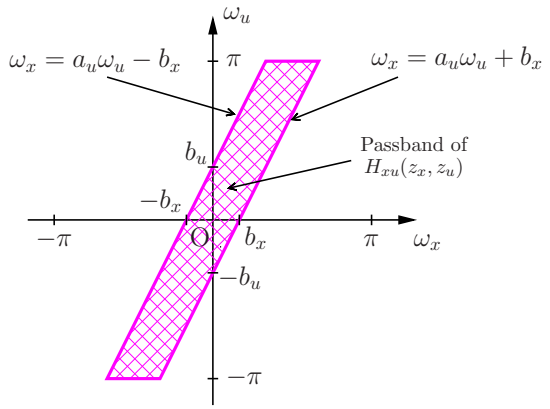

Fig. 9. Frequency-domain specifications of the ROS of $H_{xu}(z_x, z_u)$. The parameter a_u determines the orientation of the planar passband. b_x and b_u are the bandwidths of the filter along the x and u dimensions, respectively, and $b_u = b_x/a_u$.

subset of $\mathcal{B}$. Consequently, the passband of $H(\mathbf{z})$ completely encompasses the ROS of the spectrum of the object of interest. Furthermore, most of the ROSs of the spectra of interfering objects lie outside the passband of $H(\mathbf{z})$.

The filters $H_{xu}(z_x, z_u)$, $H_{yv}(z_y, z_v)$ and $H_{uvt}(z_u, z_v, z_t)$ are designed as FIR filters by employing the so-called windowing method [51](ch. 3.3). The frequency-domain specifications of the ROS of $H_{xu}(z_x, z_u)$ are shown in Fig. 9. The parameter a_u determines the orientation of the planar passband, and b_x and b_u are the bandwidths of the filter along the x and u dimensions, respectively. Note that $b_u = b_x/a_u$. The ideal infinite-extent impulse response $h^I_{xu}(n_x, n_u)$ of $H_{xu}(z_x, z_u)$ is derived in Appendix II. The finite-extent impulse response $h_{xu}(n_x, n_u)$ of $H_{xu}(z_x, z_u)$ (of order $M_x \times M_u$) is obtained as

$$h_{xu}(n_x, n_u) = h^I_{xu}(n_x, n_u)\, w_R(n_x, n_u), \qquad (32)$$

where $w_R(n_x, n_u)$ is the 2-D rectangular window of size $(M_x + 1) \times (M_u + 1)$ [51](ch. 3.3). The design of the filter $H_{yv}(z_y, z_v)$ can be carried out similar to that of $H_{xu}(z_x, z_u)$.

The velocity V_y of the object of the interest employed in the experiment is zero (hence, $k_y = 0$). In this special case, $\mathcal{B}_{uvt}$, given in (30c), is independent of the ω_v dimension. Consequently, the passband of $H_{uvt}(z_u, z_v, z_t)$ is independent of the ω_v dimension, and $H_{uvt}(z_u, z_v, z_t)$ reduces to a 2-D filter $H_{ut}(z_u, z_t)$. In fact, the finite-extent impulse response $h_{uvt}(n_u, n_v, n_t)$ can be expressed as

$$h_{uvt}(n_u, n_v, n_t) = [h^I_{ut}(n_u, n_t)\, w_R(n_u, n_t)]\, \delta(n_t), \qquad (33)$$

where $h^I_{ut}(n_u, n_t)$ can be obtained from $h^I_{xu}(n_x, n_u)$ presented in Appendix II, by replacing (n_x, n_u) with (n_u, n_t), and the parameters a_u and b_x with the counterpart parameters a_t and b_u, respectively.

C. Experimental Results

In this subsection, we present the experimental results obtained by filtering the generated LFV with the designed 5-D depth-velocity filter. The frequency specifications for the 5-D depth-velocity filter design are based on the parameterization of the decoded LFV [55] which is a two plane parameterization different than the one used for the analysis presented in Sections II and III. This leads to the filters $H_{xu}(z_x, z_u)$ and $H_{yv}(z_y, z_v)$ being designed with the parameters $a_u = a_v = -0.33$ and $b_x = b_y = 0.04$ rad/sample. The order of these filters is 8×40. The magnitude response $|H_{xu}(\mathrm{e}^{j\omega_x}, \mathrm{e}^{j\omega_u})|$ is shown in Fig. 10. A wider transition band exists along the ω_x dimension as a result of the lower order for the x dimension. Consequently, the performance in enhancing moving objects based on depth may be poor, and this fact is further discussed in Section IV-D. The magnitude response of $H_{yv}(z_y, z_v)$ is the same as that of $H_{xu}(z_x, z_u)$, which is shown in Fig. 10. A filter $H_{ut}(z_u, z_t)$ of order 40×40, designed with the parameters $a_t = -0.25$ and $b_u = 0.02$ rad/sample, is employed in the experiment. The magnitude response $|H_{uvt}(\mathrm{e}^{j\omega_u}, \mathrm{e}^{j\omega_v}, \mathrm{e}^{j\omega_t})|$ is shown in Fig. 11. Note that the much narrower transition band compared to that of $|H_{xu}(\mathrm{e}^{j\omega_x}, \mathrm{e}^{j\omega_u})|$. The order of the 5-D depth-velocity filter $H(\mathbf{z})$ is $8 \times 8 \times 80 \times 40 \times 40$.

Three frames of the original and filtered LFVs[1], corresponding to the central sub-aperture ($n_x, n_y = 5$), are shown in Fig. 12. It can be observed that the object of interest (blue car) is enhanced with slight distortion while the two interfering objects (red and orange trucks) are substantially attenuated.

[1]The complete 3-D videos corresponding to the central sub-aperture are available online at http://www.ece.uvic.ca/~panagath/research/5D-DV-F.html.

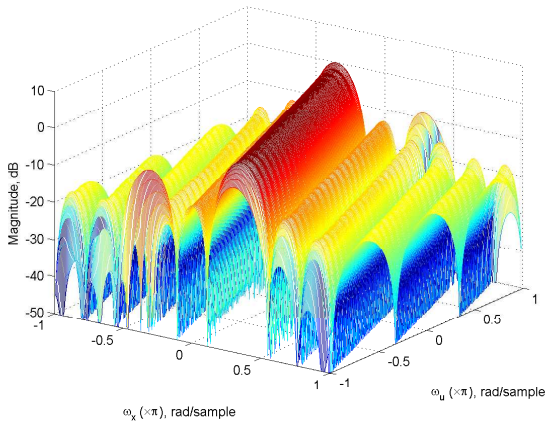

Fig. 10. Magnitude response $|H_{xu}(\mathrm{e}^{j\omega_x}, \mathrm{e}^{j\omega_u})|$ of the 2-D FIR filter $H_{xu}(z_x, z_u)$.

Most importantly, it can be seen in the 30*th frame that the object of interest, which is completely occluded in the original LFV, is considerably exposed in the filtered LFV*. Furthermore, the noise present in the original LFV is significantly attenuated by the 5-D depth-velocity filter. This is due to the fact that most of the noise energy resides in the 5-D hypervolume corresponding to the stopband of the 5-D depth-velocity filter. These results confirm the successful enhancement of the object of interest based on depth *and* velocity by the 5-D depth-velocity filter. Considering the capability of enhancing moving objects and exposing heavily occluded parts of a dynamic scene, such filters are of significant interest for applications such as digital video photography, surveillance and security systems, robotics, and various applications in computer vision.

D. Performance Limitations of Proposed 5-D Depth-Velocity Filters

In the frames of the filtered LFV, shown in Fig. 12, it can be observed that the orange truck (interfering object moving at a different depth) is less attenuated compared to the red truck (interfering object moving with a different velocity). This is mainly caused by the poor selectivity of $H_{xu}(z_x, z_u)$ and $H_{yv}(z_y, z_v)$, which primarily perform enhancement based on depth, compared to the selectivity of $H_{uvt}(z_u, z_v, z_t)$, which primarily performs enhancement based on velocity. See Figs. 10 and 11(b) for comparison. Among other factors, the selectivity of a filter is determined by the order of the filter, which in turn partly depend on the number of samples available for a particular dimension. For example, in our case, the orders of $H_{xu}(z_x, z_u)$ and $H_{yv}(z_y, z_v)$ corresponding to the x and y dimensions, respectively, cannot exceed 8 because the number of samples available for those two dimensions (or the number of sub-apertures of the available Lytro LF camera) are 9. On the other hand, the order of $H_{uvt}(z_u, z_v, z_t)$ can be as high as $40 \times 40 \times 40$ or even higher. Consequently, if the number of samples available for the x and y dimensions are comparatively low, the performance of 5-D depth-velocity filters on the enhancement of moving objects based on depth may be poor. This limitation on the highest possible order corresponding to the x and y dimensions are especially critical on the performance of FIR filters, for which substantially high orders are necessary to achieve substantial selectivity and stopband attenuation. Furthermore, the depth resolution is affected by the aperture size of the LFV camera. Consequently, in addition to the number of samples available for the x and y dimensions, a sufficiently large aperture is required for better enhancement based on depth. It is expected that the future generations of LFV cameras will offer much increased number of sub-apertures and sufficiently large apertures, which will eliminate the above mentioned drawback.

V. Discussion

A. Effects of Non-Lambertian Reflections and Occlusion

Although we assumed pure Lambertian objects in the analysis presented in Section III, in some cases, light rays emanating from a point source change with the elevation and azimuth angles. Also, except for some trivial cases, almost all real world scenes suffer from occluded objects. Consequently, if the passband of a 5-D depth-velocity filter only encompasses the ROS of the spectrum corresponding to a Lambertian object of interest with no occlusion, there may appear undesired artifacts when the real object of interest contains non-Lambertian or specular reflections and is occluded. As pointed out in [30] and [45], such artifacts may include the disappearance of non-Lambertian or specular reflections for the object of interest, the appearance of such reflections for interfering objects and the appearance of attenuated interfering objects in place of occluded parts of the object of interest. It is shown in [46] that non-Lambertian reflections and occlusion broaden the ROS of the spectrum of a Lambertian scene. Therefore, such artifacts may be alleviated by appropriately widening the passband of a 5-D depth-velocity filter so that most of the energy of the broadened spectrum resides inside the passband at the cost of reduced selectivity.

B. Enhancing Lambertian Objects Moving at Non-Constant Depth

In this subsection, we briefly discuss the enhancement of Lambertian objects moving at non-constant depth, i.e. with $V_z \neq 0$. In this case, we divide the depth range associated with the motion into small uniform segments similar to the *truncating windows* approach employed for light field rendering in [43], where depth is approximated as *piece-wise constant*. To elaborate this further, we consider the case of a Lambertian point source moving with the constant velocity $\mathbf{V} = [V_x, V_y, V_z]^{\mathrm{T}}$ as shown in Fig. 2. With the depth-segment model, the two 4-D hypersurfaces corresponding to the representation of the Lambertian point source in the LFV, $mx+u+k_xt-k_zut+c_x = 0$ and $my+v+k_yt-k_zvt+c_y = 0$ (see (12), (14a) and (14b)), may be approximated with the two *time-varying* 4-D hyperplanes

$$m(t)x + u + k_x(t)t + c_x(t) = 0 \tag{34a}$$

$$m(t)y + v + k_y(t)t + c_y(t) = 0, \tag{34b}$$

respectively, where $m(t)$, $c_x(t)$, $c_y(t)$, $k_x(t)$ and $k_y(t)$, are *piece-wise constant* with respect to the time t. They can be

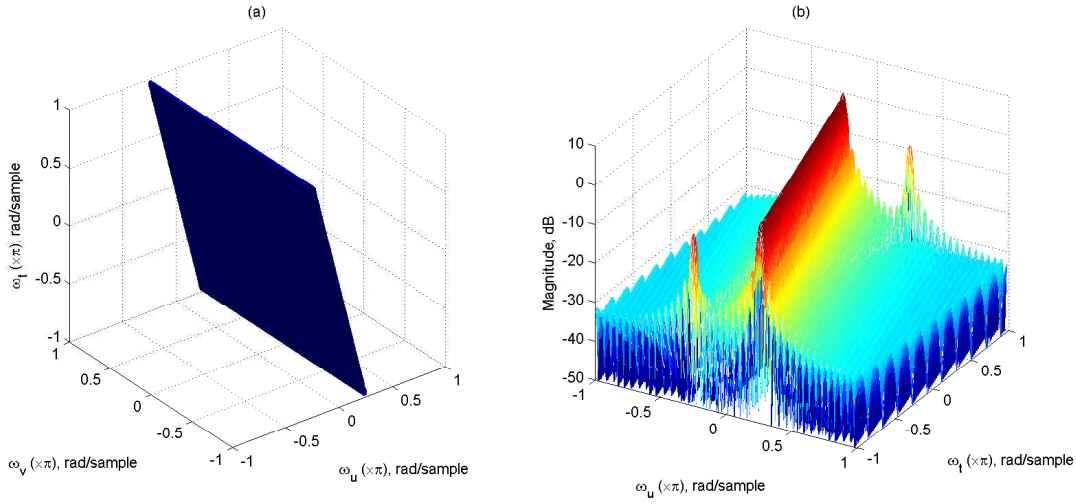

Fig. 11. Magnitude response $|H_{uvt}(\mathrm{e}^{j\omega_u}, \mathrm{e}^{j\omega_v}, \mathrm{e}^{j\omega_t})|$ of the 3-D FIR filter $H_{uvt}(z_u, z_v, z_t)$ (a) -3 dB iso-surface (b) cross section obtained at $\omega_v = 0$.

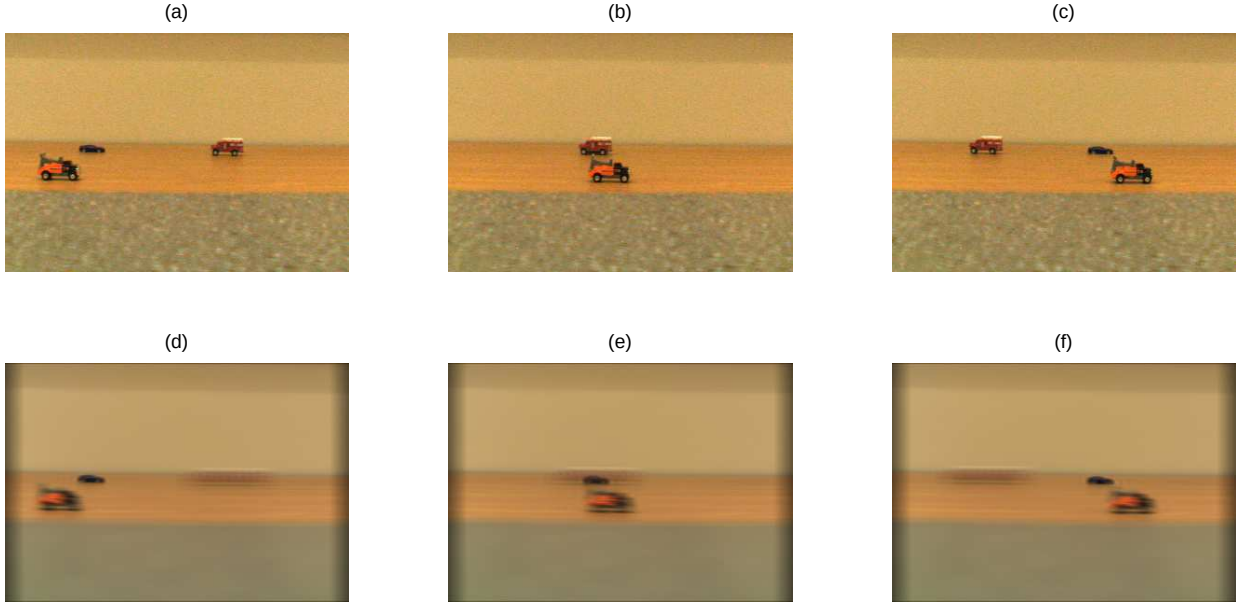

Fig. 12. Three frames of the original LFV (top row) and the filtered LFV (bottom row), $n_x, n_y = 5$; (a) and (d) 10th frame; (b) and (e) 30th frame; (c) and (f) 45th frame. The object of interest (blue car) is enhanced with slight distortion while the two interfering objects (red and orange trucks) are substantially attenuated. Note that, in the 30th frame, the object of interest is completely occluded in the original LFV and, in the filtered LFV, the object of interest is considerably exposed.

estimated using (2a), (2b), (2c), (13a) and (13b), respectively, by replacing x_0 with x_m^p, y_0 with y_m^p and z_0 with z_m^p. Here x_m^p and y_m^p are, respectively, the arithmetic mean of the x and y ranges corresponding to the pth depth segment, and z_m^p is the harmonic mean of the z range corresponding to the pth depth segment, given by

$$z_m^p = \frac{2\, d_i^p d_f^p}{d_i^p + d_f^p}, \tag{35}$$

where d_i^p and d_f^p are the initial and final values of the pth depth segment, respectively. Note that the ROS of the spectrum depends only on $m(t)$, $k_x(t)$ and $k_y(t)$ (see (19) and (20a)-(20c)), which depend on z_m^p and are independent of x_m^p and y_m^p. Because of the time-varying nature of the LFV representation, the passband of the 5-D depth-velocity filter is required to be adjusted accordingly, i.e. the 5-D depth-velocity filter should be a 5-D *adaptive* filter. The filter design can be carried out following an approach similar to the one presented in Section IV-B. However, in this case, the coefficients of the transfer functions $H_{xu}(z_x, z_u)$, $H_{yv}(z_y, z_v)$ and $H_{uvt}(z_u, z_v, z_t)$ (or the corresponding impulse responses) are functions of time rather than constants. Furthermore, for a given depth segment, the passbands of $H_{xu}(z_x, z_u)$, $H_{yv}(z_y, z_v)$ and $H_{uvt}(z_u, z_v, z_t)$ should be selected so that they encompass the 5-D hypervolumes corresponding to the *entire range* of the depth segment. For example, for the pth depth segment, the passbands should encompass the ROS given by (26) for $z_0 \in [d_i^p, d_f^p]$.

VI. Conclusions and Future Work

The spectrum of an LFV that corresponds to a Lambertian object moving with constant velocity and at constant depth is analyzed, and it is shown that such moving objects can be enhanced based on depth *and* velocity by employing 5-D depth-velocity filters. For this, a novel 5-D depth-velocity filter having a planar passband in the 5-D frequency domain is proposed and implemented. It is shown, by means of an LFV generated using a commercially available Lytro LF camera, that the proposed filter is effective in enhancing moving objects based on depth and velocity.

For the LFV employed in the experiments, the performance of the proposed 5-D depth-velocity filter in enhancing moving objects based on velocity is better compared to the performance in enhancing based on depth. This is mainly due to the limited number of sub-apertures of the available Lytro LF camera. This drawback may be partially addressed in future by the availability of next-generation LFV cameras, featuring increased sub-aperture counts.

For filtering the generated LFV, the 5-D depth-velocity filter was designed as a 5-D FIR filter. Future work includes design of appropriate 5-D IIR depth-velocity filters, which may provide lower computational complexity compared to the FIR counterparts. Furthermore, the design of 5-D depth-velocity filters that can be employed to enhance objects moving at *non-constant depths* will be considered.

Appendix I
Derivation of the Spectrum of a Lambertian Point Source Moving at a Constant Depth

The 5-D continuous-domain Fourier transform of $l_{5\mathrm{C}}(\mathbf{x})$ given in (15) can be expressed as

$$\begin{aligned} L_{5\mathrm{C}}(\mathbf{\Omega}) &= \int_{x,y,u,v,t=-\infty}^{\infty} \cdots \int l_{5\mathrm{C}}(\mathbf{x})\, \mathrm{e}^{j\mathbf{\Omega}^T\mathbf{x}}\, \mathrm{d}\mathbf{x} \\ &= \int_{x,y,u,v,t=-\infty}^{\infty} \cdots \int l_0\, \delta(mx+u+k_x t+c_x) \\ &\qquad \times \delta(my+v+k_y t+c_y)\, \mathrm{e}^{j\mathbf{\Omega}^T\mathbf{x}}\, \mathrm{d}\mathbf{x} \\ &= l_0 \int_{t=-\infty}^{\infty} L_{3\mathrm{C}}(\Omega_x,\Omega_u,t)\, L_{3\mathrm{C}}(\Omega_y,\Omega_v,t) \\ &\qquad \times \mathrm{e}^{-j\Omega_t t}\, \mathrm{d}t, \end{aligned} \tag{36}$$

where

$$\begin{aligned} L_{3\mathrm{C}}(\Omega_x,\Omega_u,t) &= \iint_{x,u=-\infty}^{\infty} \delta(mx+u+k_x t+c_x) \\ &\qquad \times \mathrm{e}^{-j(\Omega_x x+\Omega_u u)}\, \mathrm{d}u\mathrm{d}x \end{aligned} \tag{37a}$$

$$\begin{aligned} L_{3\mathrm{C}}(\Omega_y,\Omega_v,t) &= \iint_{y,v=-\infty}^{\infty} \delta(my+v+k_y t+c_y) \\ &\qquad \times \mathrm{e}^{-j(\Omega_y y+\Omega_v v)}\, \mathrm{d}v\mathrm{d}y. \end{aligned} \tag{37b}$$

Now we evaluate (37a) as

$$\begin{aligned} L_{3\mathrm{C}}(\Omega_x,\Omega_u,t) &= \iint_{x,u=-\infty}^{\infty} \delta(mx+u+k_x t+c_x) \\ &\qquad \times \mathrm{e}^{-j(\Omega_x x+\Omega_u u)}\, \mathrm{d}u\mathrm{d}x \\ &= \int_{x=-\infty}^{\infty} \mathrm{e}^{-j(\Omega_x x+\Omega_u(-mx-k_x t-c_x))}\, \mathrm{d}x \\ &= \mathrm{e}^{j\Omega_u(k_x t+c_x)} \int_{x=-\infty}^{\infty} \mathrm{e}^{-j(\Omega_x-m\Omega_u)x}\, \mathrm{d}x \\ &= 2\pi\, \delta(\Omega_x-m\Omega_u)\, \mathrm{e}^{j\Omega_u(k_x t+c_x)}. \end{aligned} \tag{38}$$

Here, we have used the fact that $\delta(mx+u+k_x t+c_x) \neq 0$ only when $mx+u+k_x t+c_x = 0$. Similarly, $L_{3\mathrm{C}}(\Omega_y,\Omega_v,t)$ can be obtained as

$$L_{3\mathrm{C}}(\Omega_y,\Omega_v,t) = 2\pi\, \delta(\Omega_y-m\Omega_v)\, \mathrm{e}^{j\Omega_v(k_y t+c_y)}. \tag{39}$$

By substituting (38) and (39) into (36), $L_{5\mathrm{C}}(\mathbf{\Omega})$ can be obtained as

$$\begin{aligned} L_{5\mathrm{C}}(\mathbf{\Omega}) &= 4\pi^2 l_0\, \delta(\Omega_x-m\Omega_u)\, \delta(\Omega_y-m\Omega_v)\, \mathrm{e}^{j(\Omega_u c_x+\Omega_v c_y)} \\ &\qquad \times \int_{t=-\infty}^{\infty} \mathrm{e}^{-j(\Omega_t-k_x\Omega_u-k_y\Omega_v)t}\, \mathrm{d}t \\ &= 8\pi^3 l_0\, \delta(\Omega_x-m\Omega_u)\, \delta(\Omega_y-m\Omega_v) \\ &\qquad \times \delta(\Omega_t-k_x\Omega_u-k_y\Omega_v)\, \mathrm{e}^{j(\Omega_u c_x+\Omega_v c_y)}. \end{aligned} \tag{40}$$

Appendix II
Derivation of the Ideal Infinite-Extent Impulse Response of $H_{xu}(z_x, z_u)$

The ideal frequency response of $H_{xu}(z_x, z_u)$, inside the principal Nyquist square of $(\omega_x, \omega_u) \in \mathbb{R}^2$, may be expressed as

$$H_{xu}(\mathrm{e}^{j\omega_x}, \mathrm{e}^{j\omega_u}) = \begin{cases} 1, & a_u\omega_u - b_x \leq \omega_x \leq a_u\omega_u + b_x \\ 0, & \text{otherwise.} \end{cases} \tag{41}$$

Then, the ideal infinite-extent impulse response $h^I_{xu}(n_x, n_u)$ of $H_{xu}(z_x, z_u)$ can be obtained, by using the 2-D Fourier series expansion of $H_{xu}(\mathrm{e}^{j\omega_x}, \mathrm{e}^{j\omega_u})$, as [51](ch. 1.3)

$$\begin{aligned} h^I_{xu}(n_x,n_u) &= \frac{1}{4\pi^2} \iint_{\omega_u,\omega_x=-\pi}^{\pi} H_{xu}(\mathrm{e}^{j\omega_x},\mathrm{e}^{j\omega_u}) \\ &\qquad \times \mathrm{e}^{j(\omega_x n_x+\omega_u n_u)}\, \mathrm{d}\omega_x\mathrm{d}\omega_u \\ &= \frac{1}{4\pi^2} \int_{\omega_u=-\pi}^{\pi} \int_{\omega_x=a_u\omega_u-b_x}^{a_u\omega_u+b_x} 1 \\ &\qquad \times \mathrm{e}^{j(\omega_x n_x+\omega_u n_u)}\, \mathrm{d}\omega_x\mathrm{d}\omega_u. \end{aligned} \tag{42}$$

After some manipulation and considering the special cases for which the denominator of $h^I_{xu}(n_x, n_u)$ is zero, the closed-form

expressions for $h^I_{xu}(n_x, n_u)$ can be obtained from (42) as

$$h^I_{xu}(n_x, n_u) = \frac{b_x}{\pi}, \quad n_x = 0 \quad \text{and} \quad n_u = 0 \tag{43a}$$

$$h^I_{xu}(n_x, n_u) = \frac{b_x \sin(n_u \pi)}{n_u \pi^2}, \quad n_x = 0 \quad \text{and} \quad n_u \neq 0 \tag{43b}$$

$$h^I_{xu}(n_x, n_u) = \frac{\sin(b_x n_x)}{n_x \pi}, \quad n_x \neq 0 \quad \text{and} \quad a_u n_x + n_u = 0 \tag{43c}$$

$$h^I_{xu}(n_x, n_u) = \frac{\sin(b_x n_x)\sin[(a_u n_x + n_u)\pi]}{n_x (a_u n_x + n_u)\pi^2}, \quad n_x \neq 0 \quad \text{and} \quad a_u n_x + n_u \neq 0. \tag{43d}$$

ACKNOWLEDGEMENT

The authors thank to Ms. Ioana Sevcenco for helping in generating the LFV used for the experiments.

REFERENCES

[1] E. H. Adelson and J. R. Bergen, "The plenoptic function and the elements of early vision," in *Computation Models of Visual Processing*, M. Landy and J. A. Movshon, Eds. Cambridge, MA: MIT Press, 1991, pp. 3–20.

[2] C. Zhang and T. Chen, "A survey on image-based rendering—representation, sampling and compression," *Signal Process.: Image Commun.*, vol. 19, no. 1, pp. 1–28, Jan. 2004.

[3] L. T. Bruton, N. R. Bartley, and Z. Q. Liu, "On the classification of moving objects in image sequences using 3D adaptive recursive tracking filters and neural networks," in *Proc. 29th Asilomar Conf. Signals, Syst., Comput.*, vol. 2, 1995, pp. 1006–1010.

[4] J.-Y. Chang, C.-C. Cheng, S.-Y. Chien, and L.-G. Chen, "Relative depth layer extraction for monoscopic video by use of multidimensional filter," in *Proc. IEEE Int. Conf. Multimedia and Expo*, 2006, pp. 221–224.

[5] S. Schauland, J. Velten, and A. Kummert, "Multidimensional linear shift invariant velocity filters for vision-based automotive applications," in *Proc. Int. Workshop Multidim. (nD) Syst.*, 2007, pp. 83–87.

[6] ——, "Detection of moving objects in image sequences using 3D velocity filters," *Int. J. Appl. Math. Comput. Sci.*, vol. 18, no. 1, pp. 21–31, Mar. 2008.

[7] ——, "Motion-based object detection for automotive applications using multidimensional wave digital filters," in *Proc. IEEE Veh. Technol. Conf. (Spring)*, 2008, pp. 2700–2704.

[8] L. T. Bruton and N. R. Bartley, "Three-dimensional image processing using the concept of network resonance," *IEEE Trans. Circuits Syst.*, vol. CAS-32, no. 7, pp. 664–672, July 1985.

[9] L. T. Bruton and N. Bartley, "The enhancement and tracking of moving objects in digital images using adaptive three-dimensional recursive filters," *IEEE Trans. Circuits Syst.*, vol. CAS-33, no. 6, pp. 604–612, June 1986.

[10] S.-C. Pei, W.-Y. Kuo, and W.-T. Huang, "Tracking moving objects in image sequences using 1-D trajectory filter," *IEEE Signal Process. Lett.*, vol. 13, no. 1, pp. 13–16, Jan. 2006.

[11] K. Kondo and N. Hamada, "Design of optimal filter for detecting linear trajectory signals utilizing object shape and velocity vector," *Electron. and Commun. in Japan, Part I*, vol. 83, no. 2, pp. 42–51, Feb. 2000.

[12] B. Anderson and L. T. Bruton, "Non-uniform bandwidth frequency-planar (NUB-FP) filter banks," in *Proc. IEEE Int. Symp. Circuits Syst.*, vol. 1, 2002, pp. I–809–I–812.

[13] B. Kuenzle and L. T. Bruton, "3-D IIR filtering using decimated DFT-polyphase filter bank structures," *IEEE Trans. Circuits Syst. I*, vol. 53, no. 2, pp. 394–408, Feb. 2006.

[14] T. Schwerdtfeger, J. Velten, and A. Kummert, "A multidimensional wave digital filter bank for video-based motion analysis," *Multidim. Syst. Signal Process.*, vol. 25, no. 2, pp. 295–311, Apr. 2014.

[15] C. U. S. Edussooriya, L. T. Bruton, and P. Agathoklis, "A low-complexity 3D spatio-temporal FIR filter for enhancing linear trajectory signals," in *Proc. IEEE Int. Conf. Acoust., Speech, Signal Process.*, 2014, pp. 1–5.

[16] M. Levoy and P. Hanrahan, "Light field rendering," in *Proc. Annu. Conf. Comput. Graph. (SIGGRAPH)*, 1996, pp. 31–42.

[17] S. J. Gortler, R. Grzeszczuk, R. Szeliski, and M. F. Cohen, "The lumigraph," in *Proc. Annu. Conf. Comput. Graph. (SIGGRAPH)*, 1996, pp. 43–54.

[18] R. Ng, M. Levoy, M. Brédif, G. Duval, M. Horowitz, and P. Hanrahan, "Light field photography with a hand-held plenoptic camera," Stanford Univ., Stanford, CA, Tech. Rep. CTSR 2005-02, 2005.

[19] R. Ng, "Fourier slice photography," in *Proc. Annu. Conf. Comput. Graph. (SIGGRAPH)*, 2005, pp. 735–744.

[20] A. Veeraraghavan, R. Raskar, A. Agrawal, A. Mohan, and J. Tumblin, "Dappled photography: Mask enhanced cameras for heterodyned light fields and coded aperture refocusing," *ACM Trans. Graph.*, vol. 26, no. 3, pp. 69–2–69–12, July 2007.

[21] A. Lumsdaine and T. Georgiev, "The focused plenoptic camera," in *Proc. IEEE Int. Conf. Comput. Photogr.*, 2009, pp. 1–8.

[22] V. Vaish, B. Wilburn, N. Joshi, and M. Levoy, "Using plane + parallax for calibrating dense camera arrays," in *Proc. IEEE Conf. Comput. Vision and Pattern Recogn.*, vol. 1, 2004, pp. I–2–I–9.

[23] V. Vaish, M. Levoy, R. Szeliski, C. L. Zitnick, and S. B. Kang, "Reconstructing occluded surfaces using synthetic apertures: Stereo, focus and robust measures," in *Proc. IEEE Conf. Comput. Vision and Pattern Recogn.*, vol. 2, 2006, pp. 2331–2338.

[24] N. Joshi, S. Avidan, W. Matusik, and D. J. Kriegman, "Synthetic aperture tracking: Tracking through occlusions," in *Proc. IEEE Int. Conf. Comput. Vision*, 2007, pp. 1–8.

[25] A. Madanayake, R. Wimalagunarathne, D. G. Dansereau, R. J. Cintra, and L. T. Bruton, "VLSI architecture for 4-D depth filtering," *Signal, Image and Video Process.*, pp. 1–10, 2013.

[26] T. Yang, Y. Zhang, X. Tong, X. Zhang, and R. Yu, "A new hybrid synthetic aperture imaging model for tracking and seeing people through occlusion," *IEEE Trans. Circuits Syst. Video Technol.*, vol. 23, no. 9, pp. 1461–1475, Sep. 2013.

[27] A. Isaksen, L. McMillan, and S. J. Gortler, "Dynamically reparameterized light fields," in *Proc. Annu. Conf. Comput. Graph. (SIGGRAPH)*, 2000, pp. 297–306.

[28] D. Dansereau and L. Bruton, "A 4D frequency-planar IIR filter and its application to light field processing," in *Proc. IEEE Int. Symp. Circuits Syst.*, vol. 4, 2003, pp. IV–476–IV–479.

[29] V. Vaish, G. Garg, E.-V. Talvala, E. Antunez, B. Wilburn, M. Horowitz, and M. Levoy, "Synthetic aperture focusing using a shear-warp factorization of the viewing transform," in *Proc. IEEE Conf. Comput. Vision and Pattern Recogn.*, 2005, pp. 129–129.

[30] D. Dansereau and L. T. Bruton, "A 4-D dual-fan filter bank for depth filtering in light fields," *IEEE Trans. Signal Process.*, vol. 55, no. 2, pp. 542–549, Feb. 2007.

[31] A. Madanayake, R. Wimalagunaratne, D. G. Dansereau, and L. T. Bruton, "Design and FPGA-implementation of 1st-order 4D IIR frequency-hyperplanar digital filters," in *Proc. IEEE 54th Int. Midwest Symp. Circuits Syst.*, 2011, pp. 1–4.

[32] R. Wimalagunarathne, A. Madanayake, D. G. Dansereau, and L. T. Bruton, "A systolic-array architecture for first-order 4-D IIR frequency-planar digital filters," in *Proc. IEEE Int. Symp. Circuits Syst.*, 2012, pp. 3069–3072.

[33] R. Wimalagunarathne, C. Wijenayake, A. Madanayake, D. G. Dansereau, and L. T. Bruton, "Integral form 4-D light field filters using Xilinx FPGAs and 45 nm CMOS technology," *Multidim. Syst. Signal Process.*, pp. 1–19, 2013.

[34] B. S. Wilburn, M. Smulski, H.-H. K. Lee, and M. A. Horowitz, "Light field video camera," in *Proc. SPIE Media Processors*, vol. 4674, 2002, pp. 29–36.

[35] B. Wilburn, N. Joshi, V. Vaish, E.-V. Talvala, E. Antunez, A. Barth, A. Adams, M. Horowitz, and M. Levoy, "High performance imaging using large camera arrays," in *Proc. Annu. Conf. Comput. Graph. (SIGGRAPH)*, 2005, pp. 765–776.

[36] S.-C. Chan, K.-T. Ng, Z.-F. Gan, K.-L. Chan, and H.-Y. Shum, "The plenoptic video," *IEEE Trans. Circuits Syst. Video Technol.*, vol. 15, no. 12, pp. 1650–1659, Dec. 2005.

[37] A. Akin, O. Cogal, K. Seyid, H. Afshari, A. Schmid, and Y. Leblebici, "Hemispherical multiple camera system for high resolution omni-directional light field imaging," *IEEE Trans. Emerg. Sel. Topics Circuits Syst.*, vol. 3, no. 2, pp. 137–144, June 2013.

[38] K. Venkataraman, D. Lelescu, J. Duparré, A. McMahon, G. Molina, P. Chatterjee, R. Mullis, and S. Nayar, "PiCam: An ultra-thin high performance monolithic camera array," *ACM Trans. Graph.*, vol. 32, no. 6, pp. 166:1–166:13, Nov. 2013.

[39] J. Neumann and C. Fermüller, "Plenoptic video geometry," *The Visual Comput.*, vol. 19, no. 6, pp. 395–404, Oct. 2003.

[40] J. Neumann, C. Fermuller, and Y. Aloimonos, “Polydioptric camera design and 3D motion estimation,” in *Proc. IEEE Conf. Comput. Vision and Pattern Recogn.*, vol. 2, 2003, pp. II–294–II–301.
[41] D. G. Dansereau, I. Mahon, O. Pizarro, and S. B. Williams, “Plenoptic flow: Closed-form visual odometry for light field cameras,” in *Proc. IEEE/RSJ Int. Conf. Intell. Robot. Syst.*, 2011, pp. 4455–4462.
[42] S.-C. Chan and H.-Y. Shum, “A spectral analysis for light field rendering,” in *Proc. IEEE Int. Conf. Image Process.*, vol. 2, 2000, pp. 25–28.
[43] J.-X. Chai, X. Tong, S.-C. Chan, and H.-Y. Shum, “Plenoptic sampling,” in *Proc. Annu. Conf. Comput. Graph. (SIGGRAPH)*, 2000, pp. 307–318.
[44] A. Levin, S. W. Hasinoff, P. Green, F. Durand, and W. T. Freeman, “4D frequency analysis of computational cameras for depth of field extension,” in *Proc. Annu. Conf. Comput. Graph. (SIGGRAPH)*, 2009, pp. 97:1–97:14.
[45] D. G. Dansereau, D. L. Bongiorno, O. Pizarro, and S. B. Williams, “Light field image denoising using a linear 4D frequency-hyperfan all-in-focus filter,” in *Proc. SPIE Comput. Imag. XI*, vol. 8657, 2013, pp. 86 570P–1–86 570P–14.
[46] C. Zhang and T. Chen, “Spectral analysis for sampling image-based rendering data,” *IEEE Trans. Circuits Syst. Video Technol.*, vol. 13, no. 11, pp. 1038–1050, Nov. 2003.
[47] M. N. Do, D. Marchand-Maillet, and M. Vetterli, “On the bandwidth of the plenoptic function,” *IEEE Trans. Image Process.*, vol. 21, no. 2, pp. 708–717, Feb. 2012.
[48] C. Gilliam, P. L. Dragotti, and M. Brookes, “A closed-form expression for the bandwidth of the plenoptic function under finite field of view constraints,” in *Proc. IEEE Int. Conf. Image Process.*, 2010, pp. 3965–3968.
[49] R. Szeliski, *Computer Vision: Algorithms and Applications*. London: Springer, 2011.
[50] Y. Wang, J. Ostermann, and Y.-Q. Zhang, *Video Processing and Communications*. Upper Saddle River, NJ: Prentice-Hall, 2002.
[51] D. E. Dudgeon and R. M. Mersereau, *Multidimensional Digital Signal Processing*. Englewood Cliffs, NJ: Prentice-Hall, 1984.
[52] R. C. Bolles, H. H. Baker, and D. H. Marimont, “Epipolar-plane image analysis: An approach to determining structure from motion,” *Int. J. Comput. Vision*, vol. 1, no. 1, pp. 7–55, 1987.
[53] Lytro, Inc. (2014) Technical specifications. [Online]. Available: https://www.lytro.com/camera/specs/
[54] B. Esfahbod. (2013) LFP File Reader (version 2.0). [Online]. Available: http://code.behnam.es/python-lfp-reader/
[55] D. G. Dansereau, O. Pizarro, and S. B. Williams, “Decoding, calibration and rectification for lenselet-based plenoptic cameras,” in *Proc. IEEE Conf. Comput. Vision and Pattern Recogn.*, 2013, pp. 1027–1034.

Chamira U. S. Edussooriya was born in Horana, Sri Lanka, in 1984. He received the B.Sc.Eng. degree in Electronic and Telecommunication Engineering (first class honors) from the University of Moratuwa, Moratuwa, Sri Lanka, in 2008 and the M.A.Sc. degree in Electrical Engineering from the University of Victoria, Victoria, BC, Canada, in 2012. He is currently working towards the Ph.D. degree in Electrical Engineering at the University of Victoria, in the area of multidimensional signal processing.

From 2008 to 2009, he worked as a Lecturer at the Department of Electronic and Telecommunication Engineering, University of Moratuwa. His Master’s thesis was nominated for the Lieutenant Governor’s Silver Medal in 2012. During his tenure as an undergraduate and a graduate student, he was awarded several scholarships including the Charles S. Humphrey Graduate Student Award in 2014. His current research interests include analysis and design of low-complexity multidimensional digital filters for plenoptic signal processing and broadband beamforming.

Donald G. Dansereau (M’05) is a research fellow with the Australian Centre for Robotic Vision, Queensland University of Technology. He completed B.Sc. and M.Sc. degrees in electrical and computer engineering at the University of Calgary in 2001 and 2004, receiving the Governor General’s Gold Medal for his Master’s work. Following industry experience including realtime physics engines and computer vision for wafer bump metrology, Donald returned to research, completing a Ph.D. in light field imaging in challenging environments at the Australian Centre for Field Robotics, University of Sydney, in 2014. Donald’s research interests are in computational and physics-based imaging and their application to challenging robotic vision problems.

Len T. Bruton (M’71-SM’80-F’81-LF’08) is a Faculty Professor of Electrical and Computer Engineering at the University of Calgary, Alberta, Canada, and an Adjunct Professor in Electrical and Computer Engineering at the University of Victoria, Victoria, B.C., Canada. He carries out research in the fields of analog and digital signal processing with emphasis on multidimensional (MD) circuits and systems and he is especially interested in the emerging applications of 2D, 3D and 4D filters for real-time directional filtering, including applications in beam forming and digital image processing. He is the inventor of a number of widely used microelectronic filtering methods, including the class of frequency dependent negative resistance (FDNR) analog filters and the class of Lossless Discrete Integrator (LDI) discrete-domain filters. He holds a number of patents.

He is a Life Fellow of the IEEE, a member of the Royal Society of Canada, a recipient of the 2002 Education Award of the IEEE Circuits and Systems Society, the 2007 Technical Achievement Award of the IEEE Circuits and Systems Society, the 50th Jubilee Medal of the IEEE Circuits and Systems Society and the 1994 Outstanding Engineer Award of IEEE Canada (Region 7) with the citation ”For leadership in engineering and the engineering profession and for research in the field of microelectronic digital and analog real-time filter design.” In Canada, he received the 1992 Manning Principal Award for Innovation and he is one of 162 scientists selected for inclusion in the textbook Great Canadian Scientists by Barry Shell, Polestar Book Publishers, 1997 (ISBN 1-896095-36-4). He received the 1992 Alberta Science and Technology Award (ASTech) for Innovation in Science in recognition of his leadership in science and in 1993 he received the Federal Government of Canada’s 125th Anniversary of Canadian Confederation Medal in recognition of his significant contributions to compatriots, community and to Canada. He is a recipient of the Centennial Award from the Alberta Association of Professional Engineers, Geologists and Geophysicists of Alberta. He has held the positions of Head of Electrical Engineering, Dean of Engineering and Vice-President Research at the University of Calgary and was the founding Dean of Engineering at the University of Victoria.

Panajotis Agathoklis (M’81-SM’88) received the Dipl. Ing. degree in electrical engineering and the Dr.Sc.Tech. degree from the Swiss Federal Institute of Technology, Zurich, Switzerland, in 1975 and 1980, respectively.

From 1981 until 1983, he was with the University of Calgary as a Post-Doctoral Fellow and part-time Instructor. Since 1983, he has been with the Department of Electrical and Computer Engineering, University of Victoria, B.C., Canada, where he is currently a Professor. His fields of interest are in control, digital signal processing and their applications. He worked in the stability of multidimensional systems and in the applications of 2D and 3D filtering.